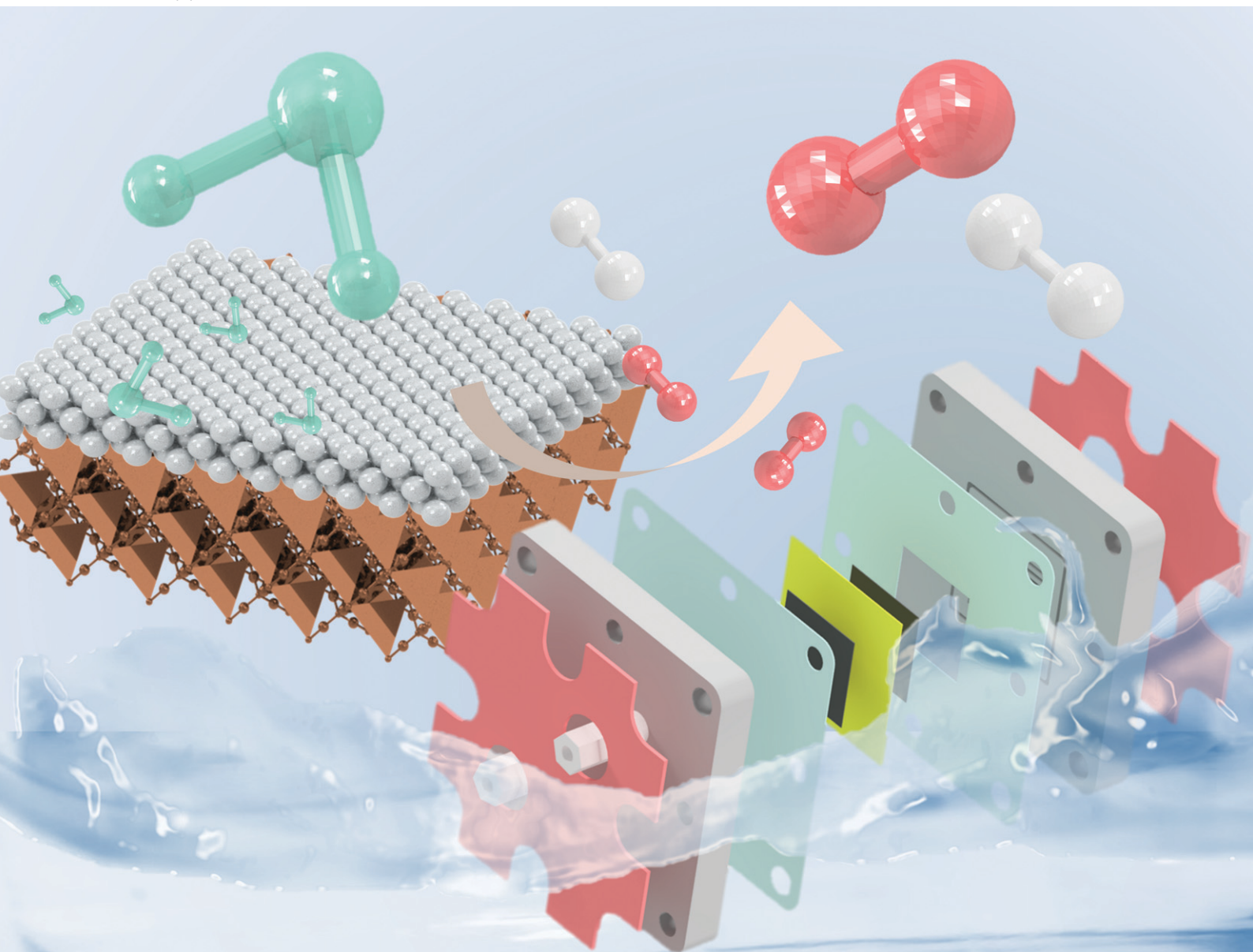


# RSC Applied Interfaces

rsc.li/RSCAppInter



ISSN 2755-3701

**PAPER**

I-Chung Cheng, Jian-Zhang Chen *et al.*  
NiMo sputter-deposition on tape-casted NiFe foam for anion  
exchange membrane water electrolysis

Cite this: *RSC Appl. Interfaces*, 2026, 3, 340

# NiMo sputter-deposition on tape-casted NiFe foam for anion exchange membrane water electrolysis

Shuo-En Yu, <sup>a</sup> I-Chung Cheng, <sup>\*b</sup>  
I-Chun Cheng <sup>c</sup> and Jian-Zhang Chen <sup>\*ade</sup>

Anion exchange membrane water electrolysis (AEMWE) offers a sustainable route for green hydrogen production. However, its large-scale deployment is constrained by the limited activity and stability of non-precious metal electrocatalysts, as well as challenges in designing efficient porous transport layers (PTLs). In this study, NiMo thin films were sputter-deposited onto tape-cast NiFe foam to construct bifunctional catalytic PTLs for AEM cells operated under both cathode-wet and cathode-dry conditions. The cell operating under cathode-wet conditions exhibited a higher current density at 1.8 V (85.5 mA cm<sup>-2</sup> at 70 °C) compared to that under cathode-dry operation (46.0 mA cm<sup>-2</sup> at 70 °C). When NiMo@NiFe foam was employed as the anode and coupled with a Ru/carbon paper (Ru/CP) cathode, the AEM cell achieved 820 mA cm<sup>-2</sup> and 784.8 mA cm<sup>-2</sup> at 1.8 V and 70 °C under cathode-dry and cathode-wet operation, respectively, outperforming the symmetric NiMo@NiFe foam system. In addition, temperature-dependent polarization analyses were conducted to investigate the temperature sensitivity of both systems. The influence of temperature on HER performance under cathode-dry operation was further discussed based on the catalytic mechanisms associated with different cathode PTLs. To evaluate the stability at an intermittent power input, an accelerated stress test (AST) was performed. The cathode-wet symmetric cell exhibited a current density decrease from 41.8 to 27.5 mA cm<sup>-2</sup> at 1.8 V after 5000 cycles at 25 °C. This work integrates sputtered NiMo with tape-cast NiFe foam as a scalable catalytic PTL design, providing insights into the effects of temperature on AEMWE operation, and the potential and remaining challenges of non-precious PTLs for practical AEMWE systems.

Received 14th November 2025,  
Accepted 11th December 2025

DOI: 10.1039/d5lf00358j

rsc.li/RSCApplInter

## Introduction

With the growing concerns over climate change and carbon emissions, reducing the reliance on fossil fuels and mitigating greenhouse gas emissions have become pressing global challenges.<sup>1</sup> Consequently, the pursuit of sustainable and clean energy sources has emerged as a critical priority. Hydrogen energy, as a clean energy carrier, shows great potential in both energy conversion and storage applications.<sup>2–4</sup> Among various hydrogen technologies, the production of green hydrogen has attracted significant

attention.<sup>5</sup> Green hydrogen is produced *via* water electrolysis powered by renewable energy sources such as wind or solar.<sup>6–8</sup> Performing the oxygen evolution reaction (OER) and hydrogen evolution reaction (HER) by using renewable energy enables hydrogen to be generated with minimal carbon emissions.<sup>9,10</sup> At the same time, owing to the intermittent nature of renewable energy sources, an efficient energy conversion method is required. Water electrolysis for hydrogen production not only involves a relatively simple system setup but also enables the conversion of electricity into hydrogen in a low-carbon process.<sup>9</sup> These advantages have driven widespread interest in the development of water electrolysis technologies.

Among various water electrolysis techniques, anion exchange membrane water electrolysis (AEMWE) has recently attracted significant attention. AEMWE combines the advantages of both alkaline water electrolysis (AWE) and proton exchange membrane water electrolysis (PEMWE). It enables the use of nonprecious metal catalysts for both the OER and HER, and it can be performed in mildly alkaline and less corrosive environments at relatively low

<sup>a</sup> Graduate School of Advanced Technology, National Taiwan University, Taipei City 106319, Taiwan. E-mail: jchen@ntu.edu.tw<sup>b</sup> Department of Mechanical Engineering, National Taiwan University, Taipei City 106319, Taiwan. E-mail: ichungch@ntu.edu.tw<sup>c</sup> Graduate Institute of Photonics and Optoelectronics and Department of Electrical Engineering, National Taiwan University, Taipei City 106319, Taiwan<sup>d</sup> Institute of Applied Mechanics, National Taiwan University, Taipei City 106319, Taiwan<sup>e</sup> Advanced Research Center for Green Materials Science and Technology, National Taiwan University, Taipei City 106319, Taiwan

temperatures.<sup>10–15</sup> However, AEMWE is still at an early stage of research, and several technical challenges need to be overcome for achieving large-scale hydrogen production. These include the development of cost-effective and high catalytic activity electrocatalysts, design of efficient porous transport layers (PTLs), reduction of material and processing costs, and improvement of system performance and long-term stability.<sup>10,11,16,17</sup>

Previous studies of electrocatalysts have reported that NiMo-based catalysts show promising activity and efficiency for the HER,<sup>18–21</sup> and NiFe-based catalysts show excellent performance and stability for the OER.<sup>22–24</sup> In NiMo-based electrocatalysts, Ni is considered to provide great catalytic activity for the HER in alkaline environments, whereas the incorporation of Mo further modifies the electronic structure of Ni, optimizing the hydrogen adsorption free energy ( $\Delta G_{H^*}$ ), which is one of the key metrics for HER performance.<sup>20,25</sup> Moreover, Ni and Mo can exhibit a synergistic effect, in which Ni facilitates the dissociation of water molecules, while Mo promotes the HER process through the hydrogen spillover effect.<sup>20,26,27</sup> On the other hand, NiFe-based materials, composed of earth-abundant and non-precious elements, offer a cost advantage.<sup>22,28–31</sup> The combination of Ni and Fe not only tunes the electronic structure of the electrocatalyst but also promotes the formation of catalytically active OER phases and interfacial species, such as metallic oxides and hydroxide/(oxy)hydroxide layers.<sup>32</sup> In addition to the catalyst performance, the substrate used as the PTLs also plays a vital role in the overall efficiency of the AEMWE cell.<sup>16</sup> The key properties of the PTLs, including electrical conductivity, contact resistance, gas and water transport capability, and chemical stability, directly influence the cell performance.<sup>33–35</sup> High conductivity and low contact resistance are essential for minimizing ohmic losses, whereas efficient gas bubble detachment significantly affects mass transport.<sup>33–35</sup> Furthermore, chemical stability under alkaline conditions determines the long-term durability of the AEMWE system.<sup>33</sup> Recent studies have indicated that the intrinsic catalytic properties of PTL substrates can contribute significantly to the overall hydrogen production performance.<sup>28,36,67,68</sup> Therefore, the design and optimization of the PTL structure and composition represent important research directions for the further development of AEMWE technology.

To address these challenges, we combined tape-casted NiFe foam and sputtered NiMo to fabricate catalytic PTLs. Tape casting is a promising method for fabricating porous, metal-based PTL substrates that could be suitable for AEMWE. It offers precise control over parameters such as the thickness, composition, and pore size, thereby facilitating the fabrication of well-structured and tunable porous alloys compatible with various catalyst designs.<sup>37,38</sup> Further, sputtering technology is widely used for the deposition of metal or metal oxide thin films. It allows precise control over the film thickness, composition, and microstructure by tuning parameters such as the deposition time, power, and

target material. Owing to its scalability and industrial applicability, sputtering holds great potential for fabricating large-area, high-performance electrode materials.<sup>39–43</sup>

In this study, a NiMo thin film was deposited *via* sputtering onto a tape-casted NiFe foam substrate and evaluated as a bifunctional electrocatalyst for both the HER and OER. Furthermore, the NiMo-coated NiFe foam was integrated into a full AEMWE cell, where it served as both the HER and OER PTLs, to assess its performance under realistic operating conditions. This study evaluates both cathode-dry and cathode-wet operations. Cathode-dry operation is a novel approach that can produce hydrogen with higher purity and lower humidity under low alkaline conditions, thus simplifying the back-of-plane (BOP) system and reducing the cost of processing the obtained hydrogen gas.<sup>44,45</sup> For comparison, a noble metal-based Ru/carbon paper (Ru/CP) cathode PTL was also evaluated to discuss the OER potential of the NiMo-coated NiFe foam, as well as to compare its HER catalytic characteristics with those of the noble metal Ru and to explore the impact of these differences on the AEMWE system performance. The reaction mechanisms were investigated by correlating electrochemical measurements with the polarization behavior of AEMWE full cells employing catalytic PTLs under both cathode-dry and cathode-wet operations. Polarization curves at different temperatures were conducted to assess the sensitivity of each configuration to temperature variations and to investigate the relationship between temperature dependence and catalytic mechanisms. Further, stability testing was conducted using an accelerated stress test (AST) with alternating high and low current loads to investigate both the intrinsic durability of the materials and their suitability for coupling with intermittent renewable energy sources.<sup>16,25,46</sup>

## Experimental section

### Pre-treatment for the tape-casted NiFe foam

Tape-casted NiFe foam was received from CellMo Materials Innovation Taiwan Inc. The foam had a thickness of approximately 0.3 mm with a porosity of 73% and was cut into 3 × 3 cm pieces. It was subjected to a pre-treatment process to clean the surface. The cut NiFe foam was first immersed in 1 M sulfuric acid and ultrasonicated for 15 min. Subsequently, it was immersed in ethanol and deionized water, each for 15 min under ultrasonication. This pre-treatment removed surface grease residues, dust particles, and undesirable oxide layers. After cleaning, the foam was dried in an oven at 70 °C for 2 h to ensure complete drying. This completed the pre-treatment.

### Sputtering NiMo metal thin film on the tape-casted NiFe foam

The pre-treated NiFe foam was then used as a substrate for NiMo metal thin film deposition (Fig. 1). DC magnetron sputtering was employed to deposit the NiMo layer. The NiFe foam was fixed on a holder, and a NiMo alloy target with a



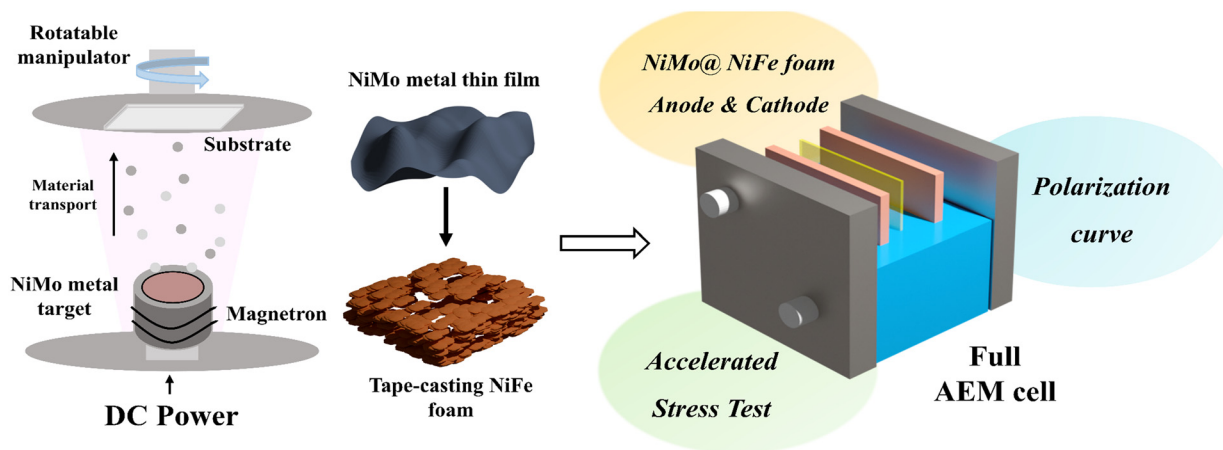


Fig. 1 Schematic illustration of the fabrication process of NiMo metallic thin film sputtered on tape-casted NiFe foam and its application in an AEMWE cell.

Ni:Mo ratio of 9:1 was used. The sputtering chamber was first evacuated to a high vacuum of  $9 \times 10^{-6}$  torr using a rotary pump followed by a turbo pump. Argon gas was then introduced into the chamber to reach a working pressure of 10 mtorr. Once the pressure stabilized, sputtering was initiated. A DC power of 80 W was applied during deposition. A 5 min pre-sputtering was conducted before deposition to stabilize the system. After that, the shutter was opened, and sputtering continued for 20 min at the same power; the deposition rate was  $\sim 1.7 \text{ \AA s}^{-1}$ . The resulting sample, with a NiMo thin film deposited on NiFe foam, was denoted as the NiMo@NiFe foam.

### Material characterization

The elemental composition, bonding environment, and oxidation states of the materials were analyzed using a hard X-ray photoelectron spectrometer (HAXPES; ULVAC-PHI Quantes) equipped with an Al  $K\alpha$  X-ray source (1.4 keV). An X-ray diffractometer (XRD; Bruker D2 PHASER) with a Cu  $K\alpha$  radiation source ( $\lambda = 0.154060 \text{ nm}$ ) was used to analyze the crystalline structure. The surface morphology was observed using scanning electron microscopy (SEM; JEOL 6500F), and energy-dispersive X-ray spectroscopy (EDS; Oxford Instruments) was employed to evaluate the elemental distribution on the surface. A goniometer (model 100SB, Sindatek) was used to assess the hydrophilicity of the surface.

### Electrochemical measurement

The catalytic activity and electrochemical properties of the electrodes for both the HER and OER were investigated using an electrochemical workstation (Autolab PGSTAT204, Metrohm, Utrecht, Netherlands). A conventional three-electrode setup was used, where Ag/AgCl, Pt, and the sample served as the reference electrode, counter electrode, and working electrode, respectively. A 1 M KOH aqueous solution was used as the electrolyte. The potential of the Ag/AgCl

reference electrode ( $E_{\text{Ag/AgCl}}$ ) was converted to the potential of the reversible hydrogen electrode ( $E_{\text{RHE}}$ ) using eqn (1):<sup>47,48</sup>

$$E_{\text{RHE}} = E_{\text{Ag/AgCl}} + 0.059\text{pH} + 0.197 \quad (1)$$

Electrochemical techniques including linear sweep voltammetry (LSV), electrochemical impedance spectroscopy (EIS), and cyclic voltammetry (CV) were employed. LSV measurements were conducted at a scan rate of  $5 \text{ mV s}^{-1}$  to obtain the polarization curves. In the LSV measurements, 90%  $iR$  compensation was applied to the measured polarization curves to minimize the effect of solution resistance ( $R_{\text{solution}}$ ) on the electrochemical results. The corrected potential was calculated using eqn (2):

$$E_{\text{corrected}} = E_{\text{measured}} - 0.9 \times I \times R_{\text{solution}} \quad (2)$$

where  $I$  is the measured current and  $E_{\text{corrected}}$  is the potential after  $iR$  compensation.<sup>49–51</sup>

EIS was carried out at overpotentials of  $-400 \text{ mV}$  and  $+400 \text{ mV}$  over a frequency range of 10 kHz to 0.1 Hz to evaluate the charge transfer resistance ( $R_{\text{ct}}$ ). CV was performed at scan rates of  $2 \text{ mV s}^{-1}$  to  $10 \text{ mV s}^{-1}$  in the potential range of  $-0.05$  to  $+0.05 \text{ V}$  (vs. Ag/AgCl) to calculate the double-layer capacitance ( $2C_{\text{dl}}$ ).

### Anion exchange membrane (AEM) cell

The AEMWE cell used in this study was purchased from Dioxide Materials (Florida, USA), and its components are illustrated in Fig. S1. The AEMWE cell consists of a symmetric structure centered on the anion exchange membrane (AEM), which is sandwiched by the catalyst-loaded PTL, flow plates with a  $5 \text{ cm}^2$  active area for fluid delivery, and a heating plate for temperature control. A Fumasep FAA-3-50 was used as the AEM; it can conduct  $\text{OH}^-$  ions. Prior to use, the membrane was activated by soaking in 1 M KOH electrolyte for 24 h. The NiMo@NiFe foam with a



size of 5 cm<sup>2</sup> was employed as the PTL on both the cathode and anode sides to evaluate its applicability in a full AEMWE cell. Additionally, a configuration using Ru/CP as the cathode PTL and NiMo@NiFe foam as the anode PTL was also tested to evaluate the OER performance of the NiMo@NiFe foam. In the AEMWE system, a peristaltic pump (DGS, DG300LN) was used to circulate the electrolyte, and a DC power supply (KIKUSUI, PWR401L) was used to control and monitor the applied voltage and resulting current.

### Preparation of the Ru/CP cathode PTL

In this study, Ru/CP was used as the cathode PTL for comparison with NiMo@NiFe foam. The Ru/CP electrode was prepared by a hydrothermal method in which Ru electrocatalysts were grown *in situ* on carbon paper. First, carbon paper (CP) with a thickness of 0.35 mm (purchased from CeTech, Taiwan) was cut into pieces of 3 × 3 cm<sup>2</sup>. The cut CP was then subjected to low-pressure plasma pretreatment to remove surface contaminants and enhance hydrophilicity. The CP was placed in a low-pressure plasma cleaner (Harrick, PDC-32G) and treated under 0.6 torr working pressure using 95% Ar and 5% O<sub>2</sub> as the working gas at a power of 11 W for 60 s. After plasma treatment, the CP was immersed in a thoroughly stirred hydrothermal precursor solution containing 1.8 mmol of RuCl<sub>3</sub>·3H<sub>2</sub>O, 20 mL of ethylene glycol, and 20 mL of deionized water. The solution and CP were then sealed inside a Teflon autoclave and heated at 160 °C for 16 h. After the reaction, the synthesized Ru/CP samples were dried and cut into pieces with an area of 5 cm<sup>2</sup>, which were then assembled into the AEM cell as the cathode PTL. The Ru/CP electrode used in this study has a mass loading of approximately 1.6 mg cm<sup>-2</sup>.

## Results and discussion

The surface morphology of NiFe foam and NiMo@NiFe foam was examined using SEM, as shown in Fig. 2. Fig. 2(a-1) to (a-4) show the morphology of the tape-casted NiFe foam. Unlike conventional metal foams, the tape-casted NiFe foam features an irregular framework with porous structures. At higher magnifications, the foam

exhibits a notably rough surface texture. Compared to commonly used metal fibers and metal foams, this rough morphology offers a larger specific surface area, which is beneficial for providing abundant electrochemically active sites. Fig. 2(b-1) to (b-4) show the morphology of the NiMo@NiFe foam after the sputter-deposition of the NiMo thin film. At lower magnification, the NiMo@NiFe foam maintains the original structural framework of the tape-casted NiFe foam, indicating that the sputtered NiMo thin film does not clog the pores, thereby preserving fluid transport pathways. At higher magnifications, the rough surface clearly becomes thicker after NiMo deposition, suggesting that the sputtered NiMo has effectively coated the irregular surface features. The inherent roughness of the NiFe foam also allows the deposited NiMo to retain a high surface area that is favorable for electrocatalysis. Elemental mapping by EDS, shown in Fig. S2, confirms the presence of Mo signals uniformly distributed across the NiFe foam, in addition to the native Ni and Fe elements.

Fig. 3 presents the XRD and XPS analysis results of the two samples. Fig. 3(a) shows the XRD patterns, where both samples exhibit peaks corresponding to  $\gamma$ -FCC austenite (JCPDS card 31-0619),<sup>52</sup> specifically the (111) and (200) crystal planes. These signals are primarily attributed to the tape-casted NiFe foam substrate. Fig. 3(b)–(g) shows the results of the XPS fine-scan spectra analysis. Fig. 3(b) and (c) show the Ni 2p spectra of the NiFe foam and NiMo@NiFe foam, respectively. The peaks at 853.9 eV and 871.9 eV correspond to Ni<sup>2+</sup> in Ni 2p<sub>3/2</sub> and Ni 2p<sub>1/2</sub>, respectively. The Ni<sup>3+</sup> peaks are located at 855.5 eV and 873.5 eV, and the metallic Ni<sup>0</sup> peak is located at 852.6 eV.<sup>48,53</sup> After sputter deposition of the NiMo thin film, the proportion of metallic Ni<sup>0</sup> increased to 4.02%, and the Ni<sup>3+</sup>/Ni<sup>2+</sup> ratio decreased from 0.35 in the original NiFe foam to 0.27 in the NiMo@NiFe foam. This reduction in the oxidation state of Ni can be attributed to the coverage of the NiMo metallic film. Fig. 3(d) and (e) show the Fe 2p spectra of the NiFe foam and NiMo@NiFe foam, respectively. The peaks at 709.6 eV and 711.8 eV, respectively, correspond to Fe<sup>2+</sup> and Fe<sup>3+</sup> in the Fe 2p<sub>3/2</sub> region.<sup>28,29</sup> The Fe<sup>3+</sup>/Fe<sup>2+</sup> ratio in the NiFe foam was calculated to be approximately 0.42. However, in the NiMo@NiFe foam, Fe signals are significantly weaker, likely owing to the surface Fe element being covered by the NiMo film, making them difficult to detect by surface-sensitive XPS. Fig. 3(f) shows the Mo 3d spectrum of the NiMo@NiFe foam. The Mo<sup>4+</sup> species exhibit peaks at 229.4 eV (Mo 3d<sub>5/2</sub>) and 232.5 eV (Mo 3d<sub>3/2</sub>), Mo<sup>5+</sup> peaks appear at 230.5 eV and 234.1 eV, and Mo<sup>6+</sup> peaks appear at 233.1 eV and 235.7 eV. Metallic Mo<sup>0</sup> is observed at 228.0 eV.<sup>54,55</sup> These results confirm the successful deposition of mixed-valence Mo species in the sputtered NiMo film.

Electrochemical measurements revealed the HER and OER catalytic activities of the NiFe foam and NiMo@NiFe foam. To enable comparison with the noble-metal catalyst Ru, the HER behavior of Ru/CP was also evaluated. Fig. 4 presents the electrochemical performance for the HER. As shown in

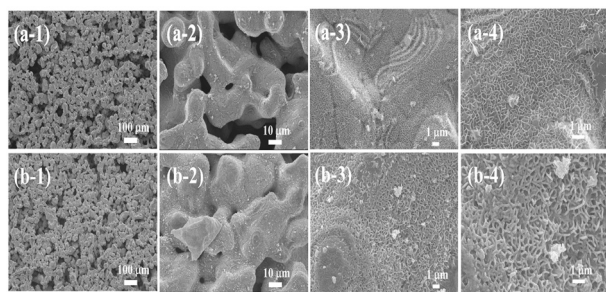


**Fig. 2** SEM images of (a-1)–(a-4): NiFe foam at magnifications of 100×, 1000×, 5000×, and 10 000×, respectively; (b-1)–(b-4): NiMo@NiFe foam at magnifications of 100×, 1000×, 5000×, and 10 000×, respectively.



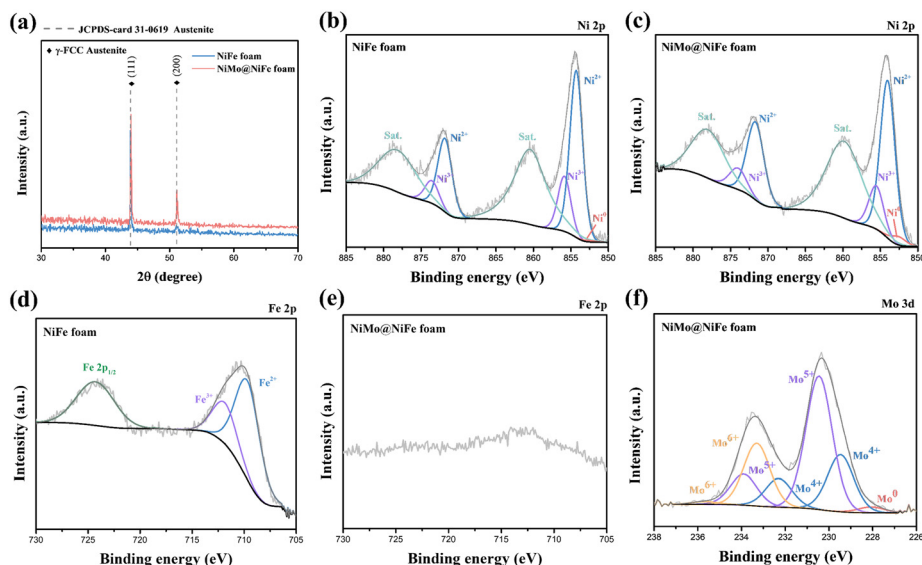


Fig. 3 Material characterization results: (a) XRD patterns; (b) and (c) Ni 2p XPS fine-scan spectra of NiFe foam and NiMo@NiFe foam, respectively; (d) and (e) Fe 2p XPS fine-scan spectra of NiFe foam and NiMo@NiFe foam, respectively; and (f) Mo 3d XPS fine-scan spectrum of NiMo@NiFe foam.

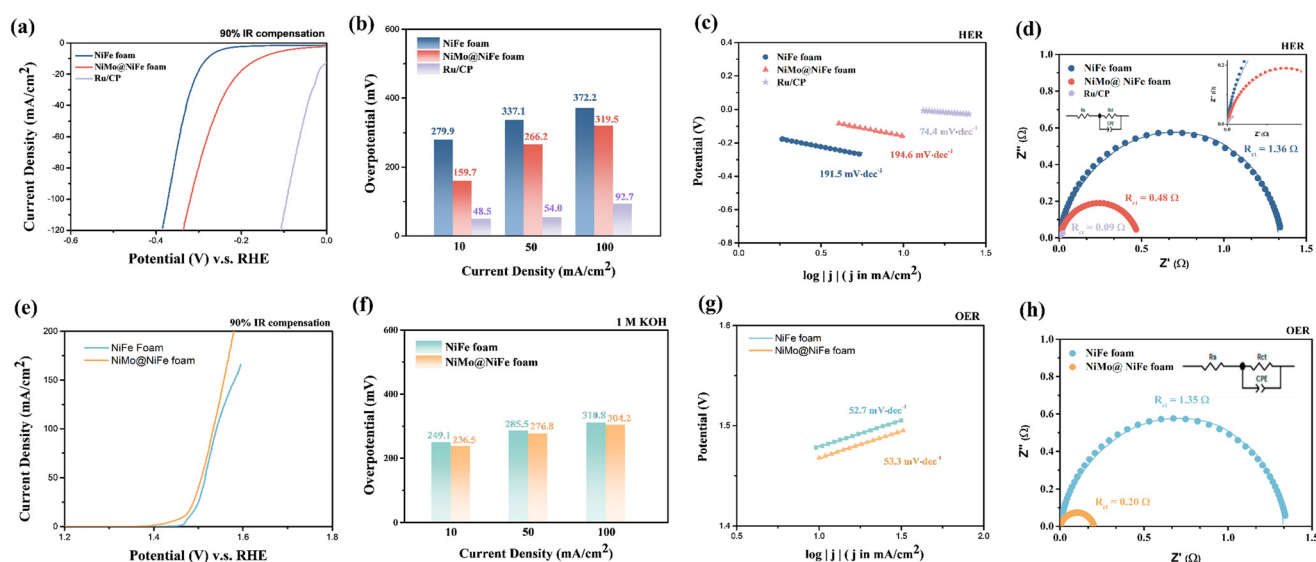
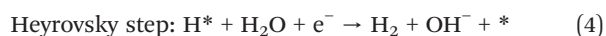


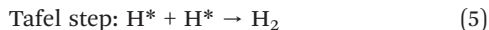
Fig. 4 Electrochemical performance of the NiFe foam, NiMo@NiFe foam, and Ru/CP electrodes for (a–d) the HER and (e–h) OER performance of the NiFe foam and NiMo@NiFe foam. (a and e) *iR*-compensated LSV curves, (b and f) overpotentials at 10, 50, and 100 mA cm<sup>-2</sup>, (c and g) Tafel slopes, and (d and h) Nyquist plots obtained from EIS measurements.

Fig. 4(a and b), the LSV results indicate that the NiMo@NiFe foam exhibits improved HER activity compared to that of the pristine NiFe foam after the NiMo metal film was deposited *via* sputtering. At current densities of 10, 50, and 100 mA cm<sup>-2</sup>, the corresponding overpotentials for the NiFe foam were 279.9 mV, 337.1 mV, and 372.2 mV, while those for the NiMo@NiFe foam were 159.7, 266.2, and 319.5 mV, respectively. These results suggest that the sputtered NiMo film contributes to lower overpotentials across different current densities, indicating superior HER catalytic performance. In contrast, the Ru/CP electrode exhibited overpotentials of 48.5, 54.0, and 92.7 mV at 10, 50, and 100

mA cm<sup>-2</sup>, respectively, indicating that there is still room for improvement in the HER performance of the NiMo@NiFe foam.

Furthermore, Fig. 4(c) shows that the NiMo@NiFe foam exhibits a similar Tafel slope (194.6 mV dec<sup>-1</sup>) to that of the NiFe foam (191.5 mV dec<sup>-1</sup>). The Tafel slope provides insight into the electrochemical kinetics, which in the HER typically involve three steps (eqn (3)–(5)):





where \* represents the active site and  $\text{H}^*$  denotes the adsorbed hydrogen intermediate.<sup>56,57</sup> Based on the Tafel slope analysis, the HER process on both the NiFe foam and NiMo@NiFe foam is mainly governed by the Volmer step as the rate-determining step (RDS). In contrast, Ru/CP shows a smaller Tafel slope of  $74.4 \text{ mV dec}^{-1}$ , suggesting that, in addition to the Volmer step, the Heyrovsky step also contributes significantly to the HER kinetics on Ru/CP.

EIS results in Fig. 4(d) show that the  $R_{\text{ct}}$  of the NiFe foam is  $1.36 \Omega$ , which significantly decreases to  $0.48 \Omega$  after NiMo film deposition. This confirms that sputtering NiMo can effectively reduce the  $R_{\text{ct}}$  and enhance the HER activity. Combining the LSV, Tafel, and impedance analyses, it can be concluded that the improvement in HER performance mainly originates from the reduction of onset potential and charge transfer resistance induced by the NiMo metallic layer, which facilitates earlier hydrogen evolution.

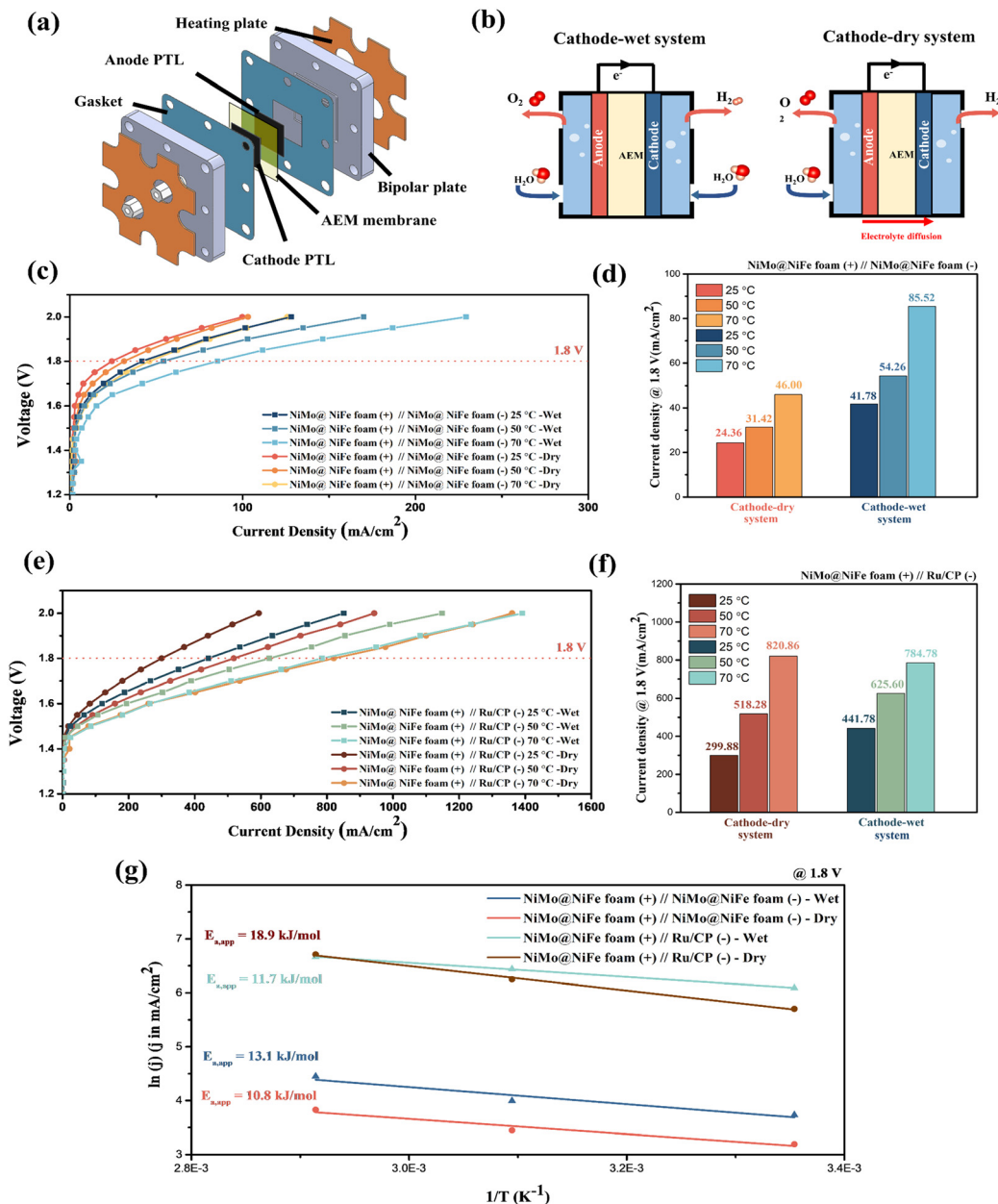


**Fig. 5** Performance evaluation of the AEM full cell: (a) schematic of the cell components, (b) illustrations of conventional cathode-wet and cathode-dry systems, (c) polarization curves with the NiMo@NiFe foam used as both the anode and cathode under different operation conditions, (d) current densities at 1.8 V under different operating conditions, (e) polarization curves with Ru/CP as the cathode and the NiMo@NiFe foam as the anode under different operation conditions, and (f) the corresponding current densities at 1.8 V with the Ru/CP cathode. (g) Arrhenius plots showing the relationship between temperature ( $1/T$ ) and current density for the calculation of the apparent activation energy ( $E_{a,app}$ ).



Fig. 4(e–h) present the electrochemical measurements for OER activity. As shown in Fig. 4(e and f), at a current density of  $10 \text{ mA cm}^{-2}$ , the overpotentials for the NiFe foam and NiMo@NiFe foam were 249.1 mV and 236.5 mV, respectively. At  $50 \text{ mA cm}^{-2}$ , the overpotentials were respectively 285.5 mV and 276.8 mV, and at  $100 \text{ mA cm}^{-2}$ , they were respectively 310.8 mV and 304.2 mV. The LSV polarization curves reveal that the OER performance of the NiMo@NiFe foam does not differ significantly from that of the pristine NiFe foam. Fig. 4(g) further shows that the NiMo@NiFe foam exhibits a comparable Tafel slope to that of the NiFe foam, suggesting similar OER kinetics, indicating that the influence of the NiMo layer on the OER remains limited. The EIS results in Fig. 4(h) reveal that the  $R_{ct}$  decreased notably from  $1.35 \Omega$  (NiFe foam) to  $0.20 \Omega$  (NiMo@NiFe foam) after NiMo sputtering, mainly due to the improved electrical conductivity of the deposited NiMo thin film. Although NiMo film deposition slightly reduces the overpotential for the OER, the improvement is far less pronounced than that observed for the HER. This indicates that the OER activity is primarily governed by the intrinsic catalytic properties of the NiFe foam, where NiFe remains the dominant active phase for the OER.

Fig. 5 presents the results of AEM full-cell performance analysis. Fig. 5(a) shows the structure of the AEM cell used in this study. The NiMo@NiFe foam was employed as both the cathode and anode PTLs, assembled with the AEM, flow field plates, and gaskets to form a complete AEM cell. In the analysis of the AEMWE system, the polarization curves were measured. Additionally, the achievable current densities under a constant input voltage of 1.8 V were compared. The energy efficiency ( $\eta$ ) of the system was further calculated using the thermal-neutral voltage ( $V_{TN}$ ) evaluated by eqn (3).<sup>28,58</sup>

$$V_{TN} = \frac{\Delta H}{nF} \quad (6)$$

where  $\Delta H$  is the enthalpy of hydrogen ( $286 \text{ kJ mol}^{-1}$ ),  $n$  is the number of electrons transferred per mole of  $\text{H}_2$  produced, and  $F$  is the Faraday constant ( $96500 \text{ C mol}^{-1}$ ). By using the experimentally measured cell voltage ( $V_{cell}$ ), the energy efficiency ( $\eta$ ) was calculated by eqn (4):

$$\eta = \frac{V_{TN}}{V_{cell}} \quad (7)$$

The measured  $V_{cell}$  and corresponding  $\eta$  values under various operating systems and conditions are summarized in Table 1.

Fig. 5(b) illustrates the AEMWE operating configurations. In the conventional cathode-wet system, an electrolyte is supplied to both the cathode and anode. In contrast, in the cathode-dry system, the electrolyte is supplied only to the anode. The electrolyte reaches the cathode *via* diffusion or wetting from the anode side, allowing the generation of low-humidity, low-alkalinity hydrogen gas.<sup>44,45</sup> This simplifies downstream hydrogen purification and reduces processing costs. In this study, we compare the performance of both operating systems at various temperatures. Fig. 5(c) shows polarization curves for the system where both electrodes use the NiMo@NiFe foam. Under all tested conditions, the performance improves with temperature owing to the enhanced electrochemical reaction kinetics. Furthermore, polarization curves indicate that the cathode-wet system consistently outperforms the cathode-dry system under identical temperature settings. Fig. 5(d) and Table 1 present the current densities at an applied voltage of 1.8 V and the required voltages to reach  $100 \text{ mA cm}^{-2}$ , along with the corresponding energy efficiencies. At  $70 \text{ }^\circ\text{C}$ , both systems show optimal performance; the cathode-dry system reaches a current density of  $46.00 \text{ mA cm}^{-2}$ , whereas the cathode-wet system reaches  $85.52 \text{ mA cm}^{-2}$ . To achieve  $100 \text{ mA cm}^{-2}$  at  $70 \text{ }^\circ\text{C}$ , the cathode-dry system requires 1.95 V ( $\eta = 75.9\%$ ), whereas the cathode-wet system only requires 1.83 V ( $\eta = 80.9\%$ ). These results confirm the superior hydrogen

**Table 1** Measured cell voltages, corresponding overpotentials ( $\eta$ ), and calculated apparent activation energies ( $E_{a,app}$ ) under various operating systems and conditions

Current density @ $100 \text{ mA cm}^{-2}$	Temperature ( $^\circ\text{C}$ )	Voltage (V)	Energy efficiency ( $\eta$ )	$E_{a,app}$ ( $\text{kJ mol}^{-1}$ )
NiMo@NiFe foam (+)/NiMo@NiFe foam (-)				
Cathode-dry	25	2.00	74.0%	11.8
	50	1.99	74.4%	
	70	1.95	75.9%	
Cathode-wet	25	1.94	76.1%	13.1
	50	1.89	78.3%	
	70	1.83	80.9%	
NiMo@NiFe foam (+)/Ru/CP (-)				
Cathode-dry	25	1.61	91.9%	18.9
	50	1.56	94.8%	
	70	1.50	98.6%	
Cathode-wet	25	1.58	93.6%	10.8
	50	1.54	96.1%	
	70	1.50	98.6%	



production efficiency of the cathode-wet system. The performance gap is likely due to the additional diffusion and wetting processes required for the electrolyte to reach the cathode in the cathode-dry configuration; this affects the water supply and HER performance. Nevertheless, while the cathode-dry system is slightly less efficient, it offers the potential advantage of producing hydrogen with higher purity and lower humidity, which is favorable for downstream hydrogen energy applications.<sup>44,45</sup>

Beyond the configuration using the NiMo@NiFe foam for both PTLs, this study further explores the anodic application potential of the NiMo@NiFe foam. For this purpose, the cathode PTL with Ru on carbon paper (Ru/CP) was replaced. Ru/CP was synthesized *via* the hydrothermal growth of Ru. The NiMo@NiFe foam (+)//Ru/CP (-) full-cell configuration allows us to evaluate the OER catalytic performance of the NiMo@NiFe foam and to compare the performance of this nonprecious-metal-based PTL with the noble-metal-based Ru/CP for the HER.<sup>59,60</sup> Fig. 5(e) shows the polarization curves under various conditions for the configuration using the NiMo@NiFe foam as the anode and Ru/CP as the cathode. As expected, the performance improves with increasing temperature, with the best performance achieved at 70 °C consistent with the enhanced reaction kinetics. According to Fig. 5(e) and (f), the cathode-wet system performs significantly better than the cathode-dry system at room temperature (25 °C). However, as the temperature increases, the gap narrows, and by 70 °C the polarization curves for both systems become nearly identical. Table 1 shows that at an input voltage of 1.8 V at 70 °C, the cathode-wet and cathode-dry systems achieved current densities of 784.78 mA cm<sup>-2</sup> and 820.86 mA cm<sup>-2</sup>, respectively. However, at higher voltage inputs like 2 V, the cathode-wet system still delivers the highest current density at 70 °C.

Notably, the influence of temperature differs between the NiMo@NiFe foam (+)//NiMo@NiFe foam (-) and NiMo@NiFe foam (+)//Ru/CP (-) systems under cathode-dry operation. In the NiMo@NiFe foam (+)//NiMo@NiFe foam (-) configuration, when the temperature is elevated during cathode-dry operation, improvements occur in electrolyte diffusion, cathode wettability, and mass transport. Consequently, the reaction rate increases with temperature, leading to enhanced overall performance. Although the performance improves, a clear difference still exists between the cathode-dry and cathode-wet operation. Even after the temperature rise enhances diffusion and wettability, the cathode-dry system still exhibits inferior polarization behavior compared with the cathode-wet system. In contrast, for the NiMo@NiFe foam (+)//Ru/CP (-) configuration, the polarization curve under cathode-dry operation also shifts toward higher current densities upon temperature elevation. When the temperature reaches 70 °C, the performance of the cathode-dry system approaches that of the cathode-wet system. These two systems, which employ different cathode PTLs, exhibit distinct sensitivities to temperature. The degree of performance enhancement upon heating and the

maximum attainable current densities under cathode-dry and cathode-wet operation differ significantly. Two possible explanations can account for the different temperature-dependent polarization behaviors.

First, for the NiMo@NiFe foam (+)//Ru/CP (-) system, the phenomenon where the performance of the cathode-dry system approaches that of the cathode-wet operation at elevated temperature may be attributed to the anodic PTL limiting the overall cell performance. Ru is a noble-metal catalyst known for its high HER activity and is considered a promising alternative to Pt.<sup>56,57</sup> In this configuration, the non-noble-metal-based NiMo@NiFe foam used as the anodic PTL may have already reached its intrinsic catalytic limit for the OER. Therefore, at lower temperatures, the cathode-dry system is constrained by electrolyte diffusion and mass transport, leading to inferior performance compared with the cathode-wet system. However, upon heating, mass transport throughout the system, especially across the interface between the cathodic PTL and AEM, is significantly improved. As a result, the Ru/CP cathode can fully utilize its catalytic capability, resulting in performance close to that of the wet operation. This explains why the NiMo@NiFe foam (+)//Ru/CP (-) system under cathode-dry conditions gradually approaches the cathode-wet operation performance as the temperature increases.

The second factor relates to the temperature sensitivity of system, which may be influenced by the intrinsic catalytic activity and reaction mechanism of the cathodic PTL itself. As shown in Fig. 5(c) and (e), the two systems exhibit different temperature-dependent polarization trends. In Fig. 5(c), for the NiMo@NiFe foam (+)//NiMo@NiFe foam (-), although the elevated temperature improves mass transport and electrolyte diffusion, the difference in performance between room temperature and 50 °C remains insignificant. Even at 70 °C, the polarization curve improves modestly but still shows a considerable gap compared to the cathode-wet system. In contrast, Fig. 5(e) shows that for the NiMo@NiFe foam (+)//Ru/CP (-), although the polarization curve under cathode-dry operation at room temperature differs greatly from that of the cathode-wet system, it becomes progressively closer as the temperature increases to 50 °C and nearly overlaps at 70 °C. Fig. 5(g) presents the relationship between temperature and current density at 1.8 V, from which the slope is used to determine the apparent activation energy ( $E_{a,app}$ ).  $E_{a,app}$  of the overall system, derived from the Arrhenius equation eqn (8) and (9):

$$j = A \cdot e^{-\frac{E_{a,app}}{RT}} \quad (8)$$

$$\ln(j) = \ln(A) + \left(-\frac{E_{a,app}}{R}\right) \cdot \frac{1}{T} \quad (9)$$

where  $j$  is the current density (mA cm<sup>-1-2</sup>),  $A$  is the Arrhenius factor,  $R$  is the gas constant (8.314 J mol<sup>-1</sup> K), and  $T$  is the absolute temperature (K).<sup>61,62</sup> Fig. 5(g) presents the relationship between temperature and current density at 1.8



V, from which the slope is used to determine  $E_{a,app}$ . The NiMo@NiFe foam (+)//Ru/CP (-) cathode-dry system exhibits the largest  $E_{a,app}$  value ( $18.9 \text{ kJ mol}^{-1}$ ), indicating that its performance is more sensitive to temperature. In contrast, the  $E_{a,app}$  values for the NiMo@NiFe foam (+)//NiMo@NiFe foam (-) system under cathode-dry and cathode-wet operation are closer ( $10.8 \text{ kJ mol}^{-1}$  and  $13.1 \text{ kJ mol}^{-1}$ , respectively) suggesting a smaller temperature dependence. This observation implies that temperature has a stronger influence on the NiMo@NiFe foam (+)//Ru/CP (-) cathode-dry system, likely due to differences in the HER mechanism and electrochemical characteristics between Ru/CP and the NiMo@NiFe foam.

In alkaline HER, Ru exhibits superior water dissociation capability and more favorable hydrogen adsorption/desorption thermodynamics compared to Ni, Mo, or Fe, with a hydrogen adsorption free energy ( $\Delta G_{H^*}$ ) value close to that of Pt in the volcano plot.<sup>56,57</sup> As shown in the Tafel analysis (Fig. 4(c)), the RDS for the NiMo@NiFe foam during the HER is the Volmer step, where water dissociation and H adsorption/desorption are kinetic bottlenecks. In contrast, Ru/CP shows a smaller Tafel slope ( $74.4 \text{ mV dec}^{-1}$ ), implying the involvement of the Heyrovsky step and faster kinetics. EIS analysis (Fig. 4(d)) further reveals that Ru/CP exhibits a much smaller  $R_{ct}$  ( $0.09 \Omega$ ) than the NiMo@NiFe foam. Therefore, in systems using the NiMo@NiFe foam as the cathodic PTL, the HER rate is limited by sluggish water dissociation and hydrogen adsorption/desorption. Although heating increases the overall reaction rate, the non-noble-metal NiMo@NiFe foam still faces an intrinsic energy barrier in the Volmer step, and its  $R_{ct}$  remains relatively high. Consequently, temperature elevation only slightly improves the cathode-dry

operation performance. Conversely, Ru/CP possesses superior water dissociation ability, smaller  $R_{ct}$ , and less limitation from the Volmer step. Elevated temperature further facilitates electron transfer during the Heyrovsky step. Thus, in the NiMo@NiFe foam (+)//Ru/CP (-) cathode-dry system, once the temperature rises and mitigates the electrolyte diffusion and mass-transport bottlenecks, the overall performance significantly improves. Meanwhile, the NiMo@NiFe foam (+)//NiMo@NiFe foam (-) configuration remains limited by water dissociation and interfacial properties, resulting in a weaker temperature-dependent enhancement. This analysis explains why the two systems exhibit distinct temperature sensitivities and why their polarization curves respond differently to temperature under cathode-dry operation.

To investigate the overall stability of the NiMo@NiFe foam in an AEM full cell, particularly under fluctuating and intermittent energy input conditions, this study employed an AST.<sup>16,46,63,64</sup> Fig. 6 presents the concept and results of the AST measurement. Fig. 6(a) illustrates the test procedure and parameters used for the AST. The measurement was performed at room temperature using a cathode-wet AEM full cell configuration. During the AST, alternating high and low current loads were applied, and after a specific number of cycles, polarization curves were measured to investigate the change in performance. Each AST cycle was defined as applying a low current load of  $0.1 \text{ A}$  for  $5 \text{ s}$  followed by a high current load of  $0.5 \text{ A}$  for another  $5 \text{ s}$ . A total of  $5000$  cycles were carried out to evaluate the AEM cell stability under intermittent current fluctuations. Fig. 6(b) shows the corresponding voltage responses at both high and low current loads. From cycle  $0$  to cycle  $1000$ , there was a noticeable increase in the voltage required for both current

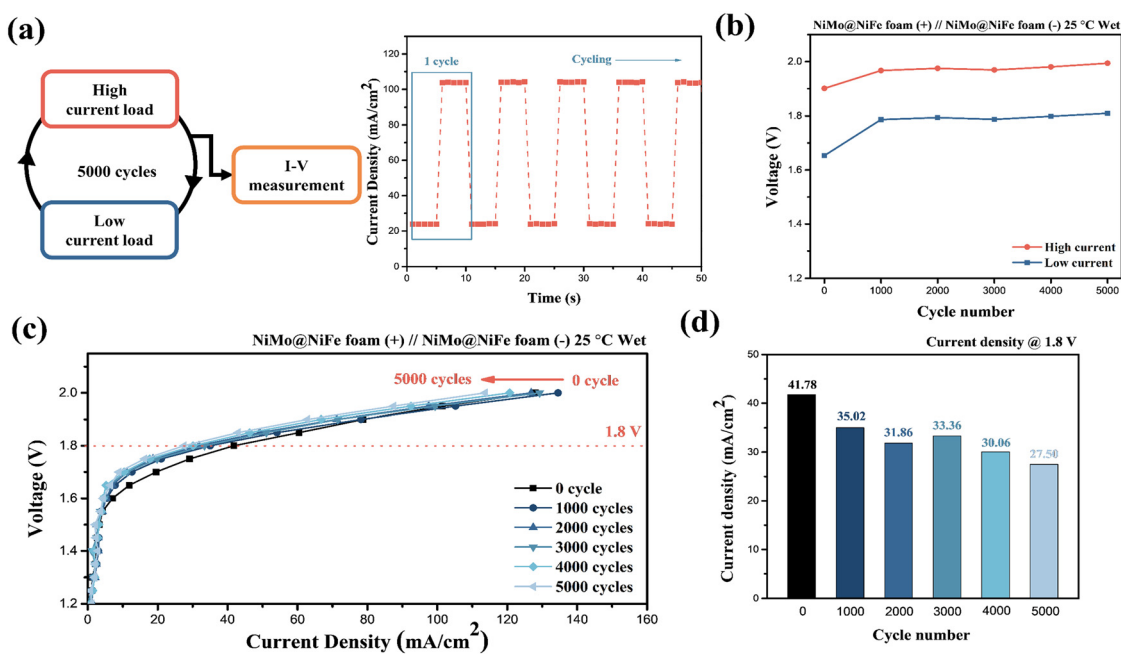


Fig. 6 AST results: (a) schematic of the AST process and current density evolution during testing, (b) voltage changes at high and low current loads under different cycle numbers, (c) polarization curves every 1000 cycles, and (d) current density at  $1.8 \text{ V}$  every 1000 cycles.



levels. However, beyond 1000 cycles, the voltage continued to increase only slightly and exhibited a more stable trend. This may be because in the early stages of the AST cycling, the material has not yet reached a stable state or is undergoing early surface reconstruction.<sup>65,66</sup>

After every 1000 cycles, the polarization curves were measured as shown in Fig. 6(c). A significant change in the polarization curve was observed after the first 1000 cycles. After 5000 cycles, the polarization curve displayed a clear decline in current density at the same applied voltage compared to the initial measurement. Fig. 6(d) provides a detailed analysis of the degradation behavior, showing the current densities corresponding to an applied voltage of 1.8 V at various cycle intervals. The trend in current density reveals a more pronounced decline after the first 1000 cycles, followed by a gradual decrease with every additional 1000 cycles. The current density decreased from an initial value of 41.78 mA cm<sup>-2</sup> to 27.50 mA cm<sup>-2</sup> after 5000 cycles, indicating a performance loss in the AEM cell. These results suggest that the AEM cell stability under dynamic load conditions can be improved further.

## Conclusions

In this study, sputtered NiMo on tape-casted NiFe foam was tested as the catalytic PTL for AEMWE. After the sputter-deposition of NiMo, the rough NiFe surface was fully covered by the NiMo metallic film. The Ni<sup>3+</sup>/Ni<sup>2+</sup> ratio in the NiMo@NiFe foam decreased from 0.35 to 0.27 owing to metal film deposition. Additionally, metallic Mo and other Mo oxidation states were detected.

In terms of electrochemical performance, the NiMo@NiFe foam exhibited improved HER catalytic activity. The overpotential at 10 mA cm<sup>-2</sup> decreased from 279.9 mV to 159.7 mV after NiMo sputtering, accompanied by a lower  $R_{ct}$  (0.48 Ω). The Tafel slopes before and after NiMo deposition remained similar (~190 mV dec<sup>-1</sup>), indicating that the RDS was still the Volmer step. For the OER, although the overpotential slightly decreased, the overall performance was comparable to that of the pristine NiFe foam, with only a reduction in  $R_{ct}$ , likely due to the enhanced conductivity introduced by the metallic layer. The dominant OER active phase remained the NiFe species within the NiFe foam.

Further investigations were conducted on the AEM full cell under different operating conditions, including cathode-dry and cathode-wet modes and varying temperatures. In the NiMo@NiFe foam (+)//NiMo@NiFe foam (-) configuration, although the cathode-dry mode theoretically produces hydrogen with lower humidity, superior performance was observed in the cathode-wet mode at 70 °C. Under 1.8 V, a current density of 85.52 mA cm<sup>-2</sup> and an energy efficiency of 80.9% were achieved. To evaluate system durability under intermittent energy input, an AST was carried out under cathode-wet conditions at 25 °C. The cell was subjected to alternating high and low current cycling. After 5000 cycles, the current density at 1.8 V decreased from 41.78 mA cm<sup>-2</sup> to

27.50 mA cm<sup>-2</sup>, indicating noticeable performance degradation.

To further explore the potential of the NiMo@NiFe foam as an OER PTL, as well as to compare the effects of different cathode PTLs under various conditions, a precious metal-based cathode (Ru/CP) was employed. In the NiMo@NiFe foam (+)//Ru/CP (-) configuration, the cathode-dry operation achieved 820.86 mA cm<sup>-2</sup>, while the cathode-wet operation reached 784.78 mA cm<sup>-2</sup> at 1.8 V and 70 °C. Ru/CP clearly outperformed the NiMo@NiFe foam as the cathode PTL in AEMWE.

The two systems exhibited distinct temperature sensitivities, particularly under dry operation. The cathode-dry system is typically limited by electrolyte diffusion and mass transport, so temperature elevation facilitates these processes. The stronger temperature dependence observed in the Ru/CP-based system can be attributed to the intrinsic HER mechanism of Ru. Meanwhile, the NiMo@NiFe foam is limited by the Volmer step and its relatively weak water dissociation ability, making temperature less influential. The Ru catalyst exhibits superior water dissociation capability and greater participation of the Heyrovsky step, which enhances the HER performance. Upon temperature elevation, the improved mass transport and electrolyte diffusion further accelerate the reaction kinetics, thereby causing the polarization curves under cathode-dry operation to exhibit higher temperature sensitivity. On the other hand, the polarization curves of the NiMo@NiFe foam (+)//Ru/CP (-) under cathode-dry and cathode-wet modes nearly overlapped at 70 °C, possibly due to the catalytic limitation at the anode PTL, which constrained the overall cell performance.

Therefore, the AEM full cell analysis highlights the strong correlation among catalyst reaction mechanisms, temperature dependence, and overall AEMWE performance. Selecting appropriate anode and cathode PTLs is thus crucial for optimizing system efficiency and stability.

## Author contributions

Shuo-En Yu: writing – review & editing, writing – original draft, validation, methodology, investigation, and formal analysis. I-Chung Cheng: supervision, resources, project administration, and methodology. I-Chun Cheng: supervision, resources, project administration, and methodology. Jian-Zhang Chen: writing – review & editing, writing – original draft, validation, supervision, resources, methodology, funding acquisition, and conceptualization.

## Conflicts of interest

The authors declare no conflicts of interest.

## Data availability

The data that support the finding of this study are available from the corresponding author upon reasonable request.



Supplementary information (SI) is available. See DOI: <https://doi.org/10.1039/d5lf00358j>.

## Acknowledgements

This work was financially supported by the “Advanced Research Center for Green Materials Science and Technology” from the Featured Area Research Center Program within the framework of the Higher Education Sprout Project by the Ministry of Education (MOE) in Taiwan (114L9006). The authors gratefully acknowledge the funding support from the National Science and Technology Council in Taiwan (NSTC 114-2221-E-002-177-MY3, NSTC 114-2218-E-002-016, and NSTC 114-2640-E-002-007). This work is also partially supported by the Industrial Technology Research Institute at Taiwan. We would like to thank CellMo Materials Innovation Taiwan Inc. for providing tape-casted NiFe foam for the experiments.

## Notes and references

- O. C. Anika, S. G. Nnabuife, A. Bello, E. R. Okoroafor, B. Kuang and R. Villa, *Carbon Capture Sci. Technol.*, 2022, **5**, 100072.
- M. El-Shafie, *Results Eng.*, 2023, **20**, 101426.
- S. Sikiru, T. L. Oladosu, T. I. Aмоса, J. O. Olutoki, M. N. M. Ansari, K. J. Abioye, Z. U. Rehman and H. Soleimani, *Int. J. Hydrogen Energy*, 2024, **56**, 1152–1182.
- D. Tang, G.-L. Tan, G.-W. Li, J.-G. Liang, S. M. Ahmad, A. Bahadur, M. Humayun, H. Ullah, A. Khan and M. Bououdina, *J. Energy Storage*, 2023, **64**, 107196.
- M. Awad, A. Said, M. H. Saad, A. Farouk, M. M. Mahmoud, M. S. Alshammari, M. L. Alghaythi, S. H. E. Abdel Aleem, A. Y. Abdelaziz and A. I. Omar, *Alexandria Eng. J.*, 2024, **87**, 213–239.
- B. Panigrahy, K. Narayan and B. Ramachandra Rao, *Mater. Today: Proc.*, 2022, **67**, 1310–1314.
- X. Li, C. J. Raorane, C. Xia, Y. Wu, T. K. N. Tran and T. Khademi, *Fuel*, 2023, **334**, 126684.
- T. Ikuerowo, S. O. Bade, A. Akinmoladun and B. A. Oni, *Int. J. Hydrogen Energy*, 2024, **76**, 75–96.
- Z. Y. Yu, Y. Duan, X. Y. Feng, X. Yu, M. R. Gao and S. H. Yu, *Adv. Mater.*, 2021, **33**, e2007100.
- S. A. Lee, J. Kim, K. C. Kwon, S. H. Park and H. W. Jang, *Carbon Neutralization*, 2022, **1**, 26–48.
- D. Hua, J. Huang, E. Fabbri, M. Rafique and B. Song, *ChemElectroChem*, 2022, **10**, e202200999.
- Y. C. Lei, J. Zhou, W. Zhou, Y. Wang, M. Zhang, A. Zhang and L. Wang, *Chem. Commun.*, 2024, **60**, 11000–11016.
- A. W. Tricker, J. K. Lee, J. R. Shin, N. Danilovic, A. Z. Weber and X. Peng, *J. Power Sources*, 2023, **567**, 232967.
- T. Wang, X. Cao and L. Jiao, *Carbon Neutrality*, 2022, **1**, 21.
- G. Sriram, K. Dhanabalan, K. V. Ajeya, K. Aruchamy, Y. C. Ching, T. H. Oh, H.-Y. Jung and M. Kurkuri, *J. Mater. Chem. A*, 2023, **11**, 20886–21008.
- A. W. Tricker, T. Y. Ertugrul, J. K. Lee, J. R. Shin, W. Choi, D. I. Kushner, G. Wang, J. Lang, I. V. Zenyuk, A. Z. Weber and X. Peng, *Adv. Energy Mater.*, 2023, **14**, 2303629.
- M.-I. Jamesh, D. Hu, J. Wang, F. Naz, J. Feng, L. Yu, Z. Cai, J. C. Colmenares, D.-J. Lee, P. K. Chu and H.-Y. Hsu, *J. Mater. Chem. A*, 2024, **12**, 11771–11820.
- J. R. McKone, B. F. Sadtler, C. A. Werlang, N. S. Lewis and H. B. Gray, *ACS Catal.*, 2013, **3**, 166–169.
- A. Nairan, P. Zou, C. Liang, J. Liu, D. Wu, P. Liu and C. Yang, *Adv. Funct. Mater.*, 2019, **29**, 1903747.
- M. Luo, J. Yang, X. Li, M. Eguchi, Y. Yamauchi and Z. L. Wang, *Chem. Sci.*, 2023, **14**, 3400–3414.
- P. Liu, W. Pan, R. Yao, L. Zhang, Q. Wu, F. Kang, H. J. Fan and C. Yang, *J. Mater. Chem. A*, 2022, **10**, 3760–3770.
- J. Zhao, J. J. Zhang, Z. Y. Li and X. H. Bu, *Small*, 2020, **16**, e2003916.
- Y. Zhou, Z. Wang, M. Cui, H. Wu, Y. Liu, Q. Ou, X. Tian and S. Zhang, *Adv. Funct. Mater.*, 2024, **34**, 2410618.
- C.-W. Su, S.-E. Yu, L.-D. Chiu, I. C. Cheng and J.-Z. Chen, *Int. J. Hydrogen Energy*, 2026, **199**, 152862.
- S.-E. Yu, C.-A. Hsu, Y.-L. Tung, C.-C. Chou, I. C. Cheng, J.-Z. Chen and P. K. Katkar, *Int. J. Energy Res.*, 2025, **2025**, 1729717.
- X. Chen, X. Wei, X. Zhang, J. Wang, Z. Wang, S. Wei, S. Liu, B. Liao, Z. Sun and X. Lu, *Green Chem.*, 2025, **27**, 4959–4985.
- E. C. J. G. Highfield and K. Oguro, *Electrochim. Acta*, 1999, **44**, 2805–2814.
- S.-E. Yu, R.-Y. Hsu, Z.-H. Pu, I. C. Cheng and J.-Z. Chen, *J. Power Sources*, 2025, **640**, 236735.
- S. E. Yu, Y. L. Su, I. C. Ni, Y. C. Chuang, C. C. Hsu, C. I. Wu, Y. S. Chen, I. C. Cheng and J. Z. Chen, *Langmuir*, 2024, **40**, 14978–14989.
- D. George and R. K. Singh, *J. Mater. Chem. A*, 2025, **13**, 38727–38752.
- S. Park, H. Choi, G. Na, H. J. Choi, D. H. Lee, M. S. Gi, J. E. Park, Y.-H. Cho and Y.-E. Sung, *J. Mater. Chem. A*, 2025, **13**, 34962–34970.
- F. Bao, E. Kemppainen, I. Dorbandt, F. Xi, R. Bors, N. Maticic, R. Wenisch, R. Bagacki, C. Schary, U. Michalczyk, P. Bogdanoff, I. Laueremann, R. van de Krol, R. Schlattmann and S. Calnan, *ACS Catal.*, 2021, **11**, 10537–10552.
- M. E. Kreider, A. R. Maldonado Santos, A. L. Clauser, M. E. Sweers, L. Hu, E. K. Volk, A. L. Chan, J. D. Sugar and S. M. Alia, *ACS Electrochem.*, 2025, **1**, 897–909.
- Q. Xu, S. Z. Oener, G. Lindquist, H. Jiang, C. Li and S. W. Boettcher, *ACS Energy Lett.*, 2020, **6**, 305–312.
- N. U. Hassan, E. Motyka, J. Kweder, P. Ganesan, B. Brechin, B. Zulevi, H. R. Colón-Mercado, P. A. Kohl and W. E. Mustain, *J. Power Sources*, 2023, **555**, 232371.
- B. Chen, A. L. G. Biancolli, C. L. Radford and S. Holdcroft, *ACS Energy Lett.*, 2023, **8**, 2661–2667.
- H. Zhao, H. Mo, P. Mao, R. Ran, W. Zhou and K. Liao, *ACS Appl. Mater. Interfaces*, 2024, **16**, 68772–68793.
- J. K. Lee, G. Y. Lau, F. Shen, A. Bergeson-Keller, X. Peng and M. C. Tucker, *J. Electrochem. Soc.*, 2024, **171**, 064505.
- F. Attar, A. Sharma, B. Gupta and S. Karuturi, *Adv. Sci.*, 2024, **11**, e2308063.



- 40 N. S. Gultom, T.-S. Chen, M. Z. Silitonga and D.-H. Kuo, *Appl. Catal., A*, 2023, **322**, 122103.
- 41 Q.-N. Ha, C.-H. Yeh, N. S. Gultom and D.-H. Kuo, *J. Mater. Chem. A*, 2024, **12**, 460–474.
- 42 T. Hrbek, P. Kúš, Y. Kostó, M. G. Rodríguez and I. Matolínová, *J. Power Sources*, 2023, **556**, 232375.
- 43 E. López-Fernández, C. Gómez-Sacedón, J. Gil-Rostra, J. P. Espinós, A. R. González-Elipse, F. Yubero and A. de Lucas-Consuegra, *Chem. Eng. J.*, 2022, **433**, 133774.
- 44 M. K. Cho, H.-Y. Park, H. J. Lee, H.-J. Kim, A. Lim, D. Henkensmeier, S. J. Yoo, J. Y. Kim, S. Y. Lee, H. S. Park and J. H. Jang, *J. Power Sources*, 2018, **382**, 22–29.
- 45 R. Wang, M. Ohashi, M. Ishida and H. Ito, *Int. J. Hydrogen Energy*, 2022, **47**, 40835–40848.
- 46 S. Natori, S. Takahashi, T. Iwataki, T. Asakawa, G. Shi, K. Kakinuma, K. Miyatake and M. Uchida, *ACS Appl. Energy Mater.*, 2025, **8**, 5823–5834.
- 47 S.-E. Yu, Y.-C. Wang, C.-Y. Tseng, I. C. Cheng and J.-Z. Chen, *Phys. Scr.*, 2024, **99**, 045605.
- 48 Z.-H. Pu, S.-E. Yu, C.-C. Hsu, I. C. Ni, C.-I. Wu, N. Devi, C.-X. Liu, Y.-S. Chen, I. C. Cheng and J.-Z. Chen, *Int. J. Hydrogen Energy*, 2025, **113**, 429–440.
- 49 A. C. Lazanas and M. I. Prodromidis, *ACS Meas. Sci. Au*, 2023, **3**, 162–193.
- 50 W. Zheng, *ACS Energy Lett.*, 2023, **8**, 1952–1958.
- 51 Y. J. Son, R. A. Marquez, K. Kawashima, L. A. Smith, C. E. Chukwunneke, J. Babauta and C. B. Mullins, *ACS Energy Lett.*, 2023, **8**, 4323–4329.
- 52 K. Saeidi, X. Gao, Y. Zhong and Z. J. Shen, *Mater. Sci. Eng., A*, 2015, **625**, 221–229.
- 53 S.-E. Yu, H.-C. Wu, I. C. Cheng and J.-Z. Chen, *J. Taiwan Inst. Chem. Eng.*, 2025, **169**, 105973.
- 54 C.-C. Chueh, S.-E. Yu, I. C. Ni, C.-I. Wu, I. C. Cheng and J.-Z. Chen, *Ceram. Int.*, 2025, **51**, 22707–22715.
- 55 C. C. Chueh, S. E. Yu, H. C. Wu, C. C. Hsu, I. C. Ni, C. I. Wu, I. C. Cheng and J. Z. Chen, *Langmuir*, 2024, **40**, 24675–24686.
- 56 Y. Li and L. Feng, *Energy Fuels*, 2023, **37**, 8079–8098.
- 57 H. Rajan, S. Anantharaj, J.-K. Kim, M. J. Ko and S. C. Yi, *J. Mater. Chem. A*, 2023, **11**, 16084–16092.
- 58 Ö. F. Selamet, F. Becerikli, M. D. Mat and Y. Kaplan, *Int. J. Hydrogen Energy*, 2011, **36**, 11480–11487.
- 59 W. Luo, Y. Wang and C. Cheng, *Mater. Today Phys.*, 2020, **15**, 100274.
- 60 Y. Li, X. Liu, J. Xu and S. Chen, *Small*, 2024, **20**, e2402846.
- 61 J. S. Ha, Y. Park, J. Y. Jeong, S. H. Lee, S. J. Lee, I. T. Kim, S. H. Park, H. Jin, S. M. Kim, S. Choi, C. Kim, S. M. Choi, B. K. Kang, H. M. Lee and Y. S. Park, *Adv. Sci.*, 2024, **11**, 2401782.
- 62 M. Menzinger and R. Wolfgang, *Angew. Chem., Int. Ed.*, 2003, **8**, 438–444.
- 63 E. Kuhnert, V. Hacker, M. Bodner and P. Subramanian, *Int. J. Energy Res.*, 2023, **2023**, 1–23.
- 64 P. Afsmann, A. S. Gago, P. Gazdzicki, K. A. Friedrich and M. Wark, *Curr. Opin. Electrochem.*, 2020, **21**, 225–233.
- 65 J. Li, W. Hu, L. Sun, L. Zhang, Q. Zhang, X. Ren and Y. Li, *Small*, 2024, **20**, e2403364.
- 66 S. Zhang, M. Cen, Q. Wang, X. Luo, W. Peng, Y. Li, F. Zhang and X. Fan, *Chem. Commun.*, 2023, **59**, 3427–3430.
- 67 L. D. Chiu, C. L. Putra, S. E. Yu, I. C. Cheng, I. C. Ni, C. I. Wu, I. C. Cheng and J. Z. Chen, *Fuel*, 2026, **411**(1), 138060.
- 68 L. D. Chiu, S. E. Yu, C. C. Chueh, I. C. Ni, C. I. Wu, I. C. Cheng and J. Z. Chen, *ACS Appl. Nano Mater.*, 2025, **8**(38), 18446–18457.

